ACS APPLIED MATERIALS & INTERFACES

RESEARCH ARTICLE

www.acsami.org

Flame Preparation of Visible-Light-Responsive $BiVO_4$ Oxygen Evolution Photocatalysts with Subsequent Activation via Aqueous Route

Yung Kent Kho,[†] Wey Yang Teoh,[†,‡] Akihide Iwase,[†] Lutz Mädler,[§] Akihiko Kudo,[⊥] and Rose Amal*[,†]

[†]ARC Centre of Excellence for Functional Nanomaterials, School of Chemical Engineering, The University of New South Wales, NSW 2052, Australia.

[‡]School of Energy and Environment, City University of Hong Kong, Hong Kong Science Park, Shatin, N.T., Hong Kong

[§]Foundation Institute of Materials Science (IWT), Department of Production Engineering, University of Bremen, 28359 Bremen, Germany

[⊥]Department of Applied Chemistry, Faculty of Science, Tokyo University of Science, Shinjuku-ku, Tokyo 162-8601, Japan

Supporting Information

ABSTRACT: Visible-light-active $BiVO_4$ photocatalyst prepared by a one-step flame spray pyrolysis demonstrates the structural evolution from amorphous to crystalline scheelite-tetragonal and further to scheelite-monoclinic (the photocatalytic active phase). Up to 95% scheelite-monoclinic content, the rest being scheelite-tetragonal, can be achieved in situ by exposing the collection filter to higher flame temperature. Reasonable activity in terms of photocatalytic O_2 evolution was obtained with the increase in crystallinity and scheelite-monoclinic content. Although analogous postcalcination of $BiVO_4$ improves crystallization and phase transformation, it inevitably induces vacancy defects that are detrimental to the photocatalytic activity. Hence a facile aqueous acid treatment on the flame-made $BiVO_4$ is introduced, which in the presence of small addition of Bi and V promotes full transformation to scheelite-monoclinic and reduces charge trapping defects. As a result, the photocatalytic O_2 evolution activity was increased by a remarkable 5 folds compared to the best performing untreated flame-made $BiVO_4$.

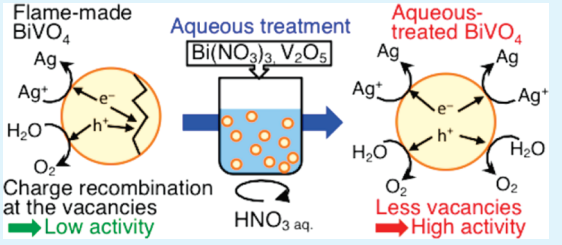

KEYWORDS: visible light photocatalyst, bismuth vanadate, nanoparticles, flame spray pyrolysis, oxygen evolution, Rietveld refinement

1. INTRODUCTION

Bismuth vanadate ($BiVO_4$) has emerged in the recent years as one of the widely investigated materials. A nontoxic and bright yellow semiconductor pigment, it has a relatively narrow bandgap that allows direct photoactivation under visible light (>420 nm). Although $BiVO_4$ has been previously exploited for a wide range of properties such as ferroeleasticity,[1] electrical conductivity,[2] optical,[3,4] and optoacoustic,[5] it is only relatively recent that $BiVO_4$ has been identified as an active photocatalyst.[6] It has since become a promising candidates for many critical green applications, such as visible light induced photochemical water splitting[7−9] and remediation of environmental pollutants.[10−12] However, $BiVO_4$ photocatalyst is very sensitive to factors such as synthesis techniques and the resultant crystal structure and defect contents.

Of the three polymorphic forms of $BiVO_4$, namely zircon-tetragonal, scheelite tetragonal, and scheelite-monoclinic, only the scheelite-monoclinic phase is reportedly active in the photocatalytic oxygen evolution.[13] Scheelite-monoclinic is the high-temperature stable phase, which can be obtained from the irreversible phase transformation of the zircon-tetragonal structure at 400−500 °C.[14] In addition, reversible phase transformation between scheelite-monoclinic and scheelite-tetragonal structures can take place at 255 °C.[14] Traditionally, $BiVO_4$ was synthesized by solid-state reaction[15] or metal−organic decomposition,[16] but because of the increased interest in photocatalytic applications, new synthesis methods such as hydrothermal treatment[17−19] and coprecipitation[14] were developed. Despite this, the difficulties in attaining precise polymorphic control of $BiVO_4$, especially for nanosized scheelite-monoclinic phase, have been elusive and present a major challenge. The scheelite-monoclinic phase is often associated with bulk (micrometer) particle size, which helps to stabilize the nonright angle of the monoclinic unit-cell structure.[14−19]

Recently, Strobel et al. introduced the flame spray synthesis of $BiVO_4$ powders as bright yellow pigments, and further encapsulate in SiO_2 (in the same preparation step) to prevent thermal sintering as well as to suppress photocatalytic activity.[20] However, its photocatalytic performance was not assessed, and especially so since the powders were targeted for applications as pigments,

Received: February 27, 2011
Accepted: May 5, 2011
Published: May 05, 2011

where photocatalytic activity is undesired. The photocatalytic activity of similarly made powder was assessed by Castillo et al., showing only moderate photoactivity.[21] However, the exact crystal phase (most likely a mixture of scheelite-monoclinic and scheelite-tetragonal) was not resolved and quantified precisely, preventing hence the elucidation of structural-performance relationship.

In this work, we investigate the amorphous and polymorphic evolution of $BiVO_4$ nanocrystals during the synthesis by flame spray pyrolysis (FSP). In general, FSP is a convenient technique for synthesizing nanocrystalline particles (<100 nm),[22] an elusive characteristic for active phase $BiVO_4$ by most wet techniques. By applying careful crystallographic phase refinement to differentiate between the otherwise indistinguishable scheelite-monoclinic and scheelite-tetragonal phases, we were able to follow the polymorphic evolution of $BiVO_4$. Such refinement was further critical in establishing the relationship between the physicochemical characteristics and the photocatalytic efficiency, especially in aqueous O_2 evolution. By identifying the critical physicochemical characteristics, a novel aqueous-based acid treatment of the as-prepared $BiVO_4$ is introduced in this work to significantly improve its photocatalytic activity.

2. EXPERIMENTAL METHOD

2.1. Flame Synthesis of $BiVO_4$ Photocatalysts and Acid Modification. Liquid precursors consisting of 0.25 M each of Bi and V were prepared by mixing bismuth precursor and vanadium oxytripropoxide (97%, Aldrich) in xylene (Raedel-de-Haen). Bismuth precursor was obtained by dissolving bismuth acetate (99.99+%, Aldrich) in 2-ethylhexanoic acid (Aldrich) and refluxing for 6 h. During the flame synthesis, 10 mL min^{-1} of liquid precursor was delivered to the FSP nozzle using a syringe pump (Inotech R232), and dispersed by 5 L min^{-1} of O_2 at 1.5 bar.[23] The dispersed precursor droplets was ignited by a surrounding oxygen-methane flame (3.2 L min^{-1} O_2, 1.5 L min^{-1} CH_4). Additional 5 L min^{-1} of sheath O_2 was provided through the outermost metal ring. $BiVO_4$ aerosols were collected on glassfibre filter (Whatmann GF/D), with the aid of a vacuum pump (Alcatel SD series). A K-type thermocouple was placed in front of the filter to measure the exposed filter temperature (T_f) during FSP synthesis.[20] The T_f is the asymptotically maximum filter temperature achieved by controlling the burner-filter distance (BFD).[20] Particles synthesis and collections were carried out for 15 min.

An aqueous-based treatment was employed to modify flame-made $BiVO_4$ powders. Here, suspension containing 0.5 g of $BiVO_4$ powder in 50 mL of 0.75 M HNO_3 solution was magnetically stirred at 1200 rpm, in a baffle flask for 48 h. In some cases, extra Bi as $Bi(NO_3)_3.5H_2O$ (0.5 mmol) and V precursors as V_2O_5 (0.25 mmol) were added. The suspended particles were recovered by filtration and washed with milli-Q water prior to drying in air.

2.2. Characterization and Photoelectrochemical Measurement of $BiVO_4$ Particles. X-ray diffraction (XRD) of the $BiVO_4$ powders was carried out on Phillips X'pert MPD using Cu Kα radiation operating at 45 kV, 40 mA and scanning from 10 to 65° with step size of 0.02°. An array detector was used for collecting the diffraction signals. The XRD patterns were analyzed by Rietveld refinement using the commercial PANalytical X'pert HighScore Plus software. The amount of amorphous content was deduced by the area under the curvature hump of the XRD baseline using the software. Raman spectra were collected on Renishaw inVia Raman Microscope equipped with green laser line (514 nm). The Raman spectrometer was operated at 2.5 mW cm^{-2}, scanning from 1000 to 200 cm^{-1}. Specific surface areas (SSA) of the particles were measured on Micromeritics Tristar 3000 by nitrogen adsorption at 77 K according to the Brunauer–Emmett–Teller (BET) method. The powder samples were pretreated in Micromeritics VacPrep unit at 150 °C for at least 1 h before measurements. Transmission electron microscope images were obtained on TEM Phillip CM200, operating at 200 kV. The UV–vis diffuse-reflectance spectra were obtained on Varian Cary 5 UV–vis–NIR spectrophotometer and converted to absorbance by the Kubelka–Munk method.

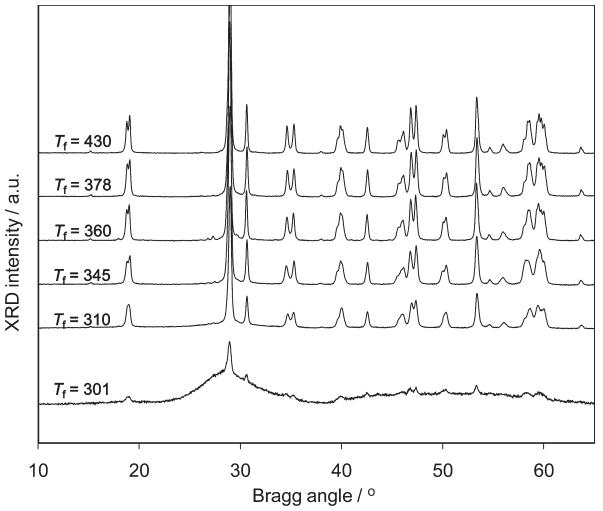

Figure 1. XRD patterns of flame synthesized $BiVO_4$ nanoparticles at various exposed particle filter temperatures (in °C).

Thin films of $BiVO_4$ were prepared by mixing 0.1 g of powder with acetylacetone (10 μL) and water (100 μL) in an agate mortar and pestle. The resulting paste was coated onto ITO conductive glass by doctor blading, and dried at 100 °C for 6 h. Photoelectrochemical (PEC) measurements were carried out in a standard three electrode system, with Pt counter electrode and Ag/AgCl reference electrode, while a 300 W Xe lamp was used as the illumination source. Electrolyte medium consisting of 0.1 M Na_2SO_4 aqueous solution was continuously purged with N_2 before and during the PEC measurements. The photocurrents were recorded with an Autolab PGSTAT12 potentiostat at scan speed of 0.02 V s^{-1}.

2.3. Photocatalytic Oxygen Evolution. Photocatalytic oxygen evolution was carried out in a closed gas circulation system.[8] The dead volume of the reactor is 240.5 mL. $BiVO_4$ powders (0.3 g) were dispersed and magnetically stirred in 150 mL of aqueous solution containing 0.05 M $AgNO_3$. Prior to photocatalytic O_2 evolution, the suspension was evacuated for 30 min to remove dissolved gases. Visible light irradiation was provided by 300 W Xe lamp using a 420 nm cut off filter and delivered from the top of the cell through a Pyrex window. The amount of oxygen evolved was measured using an online gas chromatograph (Shimadzu, GC-8A, TCD).

3. RESULTS AND DISCUSSION

3.1. Formation of Flame-Synthesized $BiVO_4$ and Physical Characteristics. As shown from the XRD pattern in Figure 1, the $BiVO_4$ nanoparticles evolve from amorphous to increasing crystallined samples with higher collection temperature on filter (T_f). The degree of crystallinity of the as-prepared samples, increases from 9, 70, 92 to 100% simply by varying the exposed T_f from 301, 310, 345 and >360 °C, respectively (see Table 1). The slightly crystallined content at T_f = 301 °C is in agreement with the Tamman temperature of $BiVO_4$ which occurs at 300 °C. That crystallization of the initially predominant amorphous $BiVO_4$ occurs as a function of T_f implies that the rapid flame residence

Table 1. Rietveld Analysis of Flame-Synthesized and Aqueous HNO_3 Solution-Modified $BiVO_4$ Nanoparticles

sample	T_f (°C)	BFD (cm)	crystallinity (wt %)[a]	scheelite-monoclinic phase (wt %)[b]	R_{exp}[c]	R_{wp}[c]	GOF[c]
1	301	56.3	9				
2	310	73.5	70	73	1.82	4.66	6.5
3	345	69.5	92	80	1.80	7.09	15.5
4	360	65.5	100	89	1.80	6.74	14.0
5	378	73.5	100	82	1.85	6.61	13.4
6	430	73.5	100	95	1.84	6.53	12.5

	modified samples[d]	solution	crystallinity (wt %)[a]	scheelite-monoclinic phase (wt %)[b]	R_{exp}[c]	R_{wp}[c]	GOF[c]
7	$mBiVO_4$-1a	HNO_3(aq.) only	100	85	1.82	7.47	16.8
8	$mBiVO_4$-1b	HNO_3(aq.) + Bi + V	100	100	1.86	8.97	22.6
9	$mBiVO_4$-2b	HNO_3(aq.) + Bi + V	100	100	1.76	8.64	22.9

[a] Crystallinity = 100% − amorphous content (%). Amorphous content was deduced by the area under curvature hump of the XRD baseline. [b] Fraction of scheelite-monoclinic in crystallite content of $BiVO_4$. Fraction of scheelite-tetragonal in crystallite content = 100% − scheelite-monoclinic phase. [c] Rietveld refinement agreement indices (see the Supporting Information). [d] Convention of labeling for modified sample: 1 − amorphous starting material, 2 − crystallined starting material, a − treatment with aqueous HNO_3, b − treatment with aqueous HNO_3 + Bi + V.

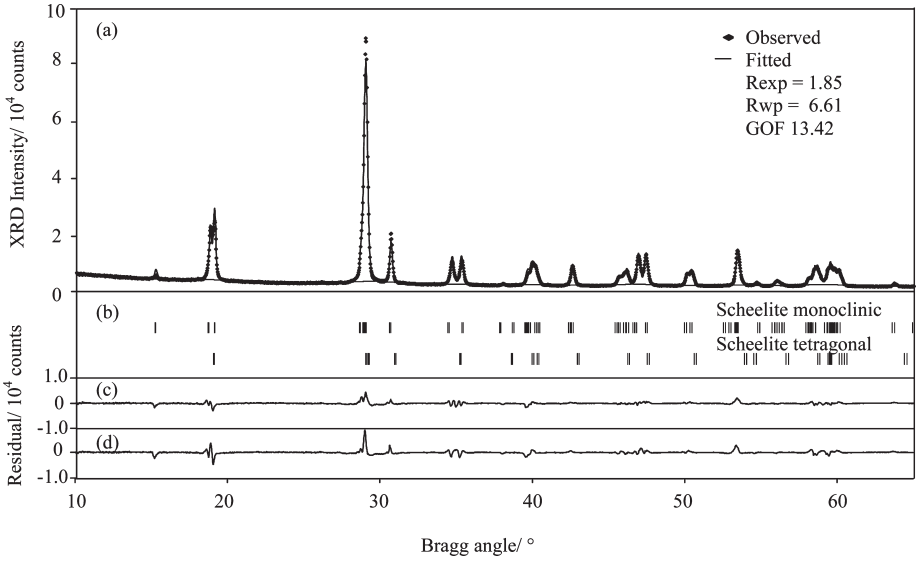

Figure 2. (a) Rietved refinement for $BiVO_4$ powder (T_f = 378 °C); (b) reference peaks from the inorganic crystal structure database (scheelite-monoclinic ICSD: 100603, scheelite-tetragonal ICSD: 062706); (c, d) residual plot between fitted and observed intensity for scheelite-monoclinic and scheelite tetragonal, respectively.

time (order of milliseconds) was insufficient to induce crystallization within the flame. This is further prompted by the late $BiVO_4$ nucleation at the downstream of the flame, driven by its relatively low boiling point of 922 °C, similar to the temperature of the tip of a spray flame.[24]

As further deduced by Rietveld refinement (Table 1), in situ crystallization of $BiVO_4$ on the filter is accompanied by phase transformation from scheelite-tetragonal to scheelite monoclinic. Although the existence of scheelite-monoclinic phase at high T_f is readily discernible from the peak splitting diffractions[14,25] at 2θ = 18.5, 35, and 46° (Figure 1), they are difficult to distinguish from the scheelite-tetragonal phase. The presence of scheelite-tetragonal phase could result, for example, in the more intense second peak at the peak split at 18.5°. As such, careful analysis of the diffraction pattern by Rietveld refinement is required to distinguish between the two crystal phases with overlapping diffractions. Figure 2 shows a representative Rietveld refinement profile for flame synthesized $BiVO_4$ powder (T_f = 378 °C). During the refinement process, coexistence of scheelite-monoclinic and scheelite-tetragonal phases (Figure 2b) was taken into consideration. Rietveld analysis shows indeed that significant scheelite-tetragonal crystallite content (18%) is present for as-collected $BiVO_4$ (T_f = 378 °C). Crystallinity and phase composition of flame synthesized $BiVO_4$ particles at different T_f is further given in Table 1. While the crystallinity of $BiVO_4$ nanoparticle gradually improves with increasing T_f from 301 to 430 °C, the fraction of scheelite-monoclinic phase in the crystallite content also increases from 73 to 95%, respectively, in agreement with the reversible high-temperature stable phase expected for scheelite-monoclinic at above 255 °C.[14]

The improved crystallinity as a result of sintering is prompted by the increase in crystallite sizes, d_{XRD} from 47 to 71 nm with increasing T_f (Table 2). The increasing d_{XRD} is attributable to the growth of both scheelite particles. It is observed that the

Table 2. Crystallite Sizes ($d_{s\text{-}m}$, $d_{s\text{-}t}$, and d_{XRD}, respectively, for scheelite-monoclinic, scheelite-tetragonal phases, and weighted-average crystallite size), Specific Surface Areas (SSA), and SSA-Equivalent Particle Diameter of $BiVO_4$ Nanoparticles

sample	T_f (°C)	$d_{s\text{-}m}$ (nm)[a]	$d_{s\text{-}t}$ (nm)[a]	d_{XRD} (nm)[b]	d_{ssa} (nm)[c]	SSA (m^2g^{-1})
1	301				30	28
2	310	47	47	47	48	18
3	345	49	55	50	62	14
4	360	62	67	62	72	12
5	378	64	66	64	86	10
6	430	71	75	71	123	7
7	$mBiVO_4$-1a	69	78	70	123	7
8	$mBiVO_4$-1b	72		72	108	8
9	$mBiVO_4$-2b	103		103	143	6

[a] Crystallite size of scheelite-monoclinic and scheelite-tetragonal particles obtained by Rietveld refinement. [b] Weighted-average crystallite size, d_{XRD} = scheelite-monoclinic (wt %) × $d_{s\text{-}m}$ + scheelite-tetragonal (wt %) × $d_{s\text{-}t}$. [c] $d_{SSA} = 6/(\rho_{BiVO4} \times SSA)$.

crystallite size of scheelite-tetragonal phase ($d_{s\text{-}t}$) is always larger than that of scheelite-monoclinic ($d_{s\text{-}m}$) (Table 2), inferring that both thermal and sintering-induced phase transformation took place. It is possible that smaller crystals of scheelite-monoclinic were precipitated out from sheelite-tetragonal as the latter sinters. The consistently larger specific surface areas (SSA)-equivalent diameter, d_{SSA}, compared to d_{XRD} further infers the presence of interparticle necking as a result of loss in external surface area at the necking interface (Table 2).[26] In fact, severe necking between particles could be observed by TEM analysis (Figure 3), whereas the primary particle sizes were in qualitative approximation with that deduced by d_{XRD}.

The Raman spectra of as-collected flame-made $BiVO_4$ powders gave information on the local structures of vanadium−oxygen bonding (Figure 4). The Raman bands observed at 324 and 366 cm^{-1} for all samples are characteristics to the deformation of VO_4^{3-} tetrahedron,[27,28] whereas Raman stretching around 826 and 710 cm^{-1} gives information on the vanadium−oxygen bond lengths.[29,30] The V−O bond length is affected by the Bi^{3+} ion positions and hence is a good indicator for the unit-cell structure and the distortion of the overall framework of the $BiVO_4$ unit cell.[19] As shown in Figure 4, the peak positions at ~826 cm^{-1} for different $BiVO_4$ samples are systematically shifted to lower band frequencies with increasing T_f. The shoulder at 710 cm^{-1} becomes more distinct with increasing T_f. The position of the most intense Raman peak (~826 cm^{-1}) and its V−O bond length is given in Table 3. Here, the bond length is generally shorter (1.689 Å, Raman band 835 cm^{-1}) in less crystalline (91% amorphous) $BiVO_4$ particles, but becomes longer (1.964 Å, Raman band 827 cm^{-1}) as the crystallinity increases (100% crystalline, T_f = 430 °C). Note that the shifting in the maxima in Raman band maxima is taken as representation of the average bond length in relative term, rather than absolute. Although varying V−O bond distances were also reported for $BiVO_4$ (scheelite-monoclinic structure) synthesized by hydrothermal method and were attributed to different particle morphology (1.696 Å for large crystals and 1.708 Å for rodlike-grain particle),[19] the different V−O bond length observed here is mainly attributed to the less well-defined amorphous bonds (Figure 4).

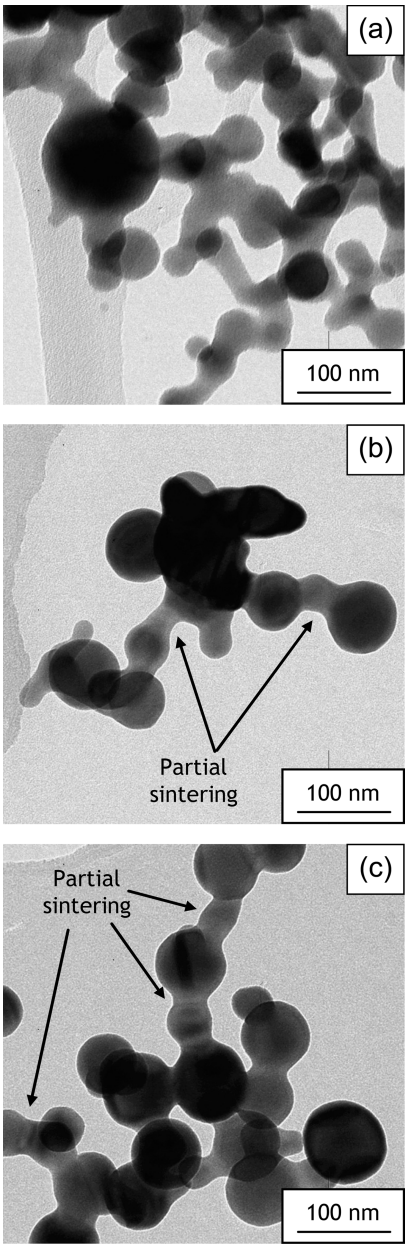

Figure 3. TEM images illustrating partial sintering of $BiVO_4$ on the filter paper, resulting in necked particles; T_f = 345 (a); 378 (b); and 430 °C (c).

Despite the presence of the scheelite-tetragonal phase in the bulk of $BiVO_4$ (T_f = 310−378 °C) as observed by XRD, Raman spectra did not find corresponding V−O bond (or peak maxima 788 cm^{-1}) on the surface, which otherwise correspond to that of scheelite-tetragonal structure. Note that in this particular instance, the surface is defined as the penetration depth of Raman spectroscopy, whereas the XRD given its higher penetration depth gives information of the bulk. Such observation infers that phase transformation of scheelite-tetragonal to scheelite-monoclinic begins on the $BiVO_4$ surface, and slowly extends into the bulk of the particles. This agrees well with the increased crystallinity and scheelite-monoclinic content with increasing T_f.

All $BiVO_4$ powders show optical absorption in the visible light region up to 520 nm (Figure 5). The bandgap energy of $BiVO_4$

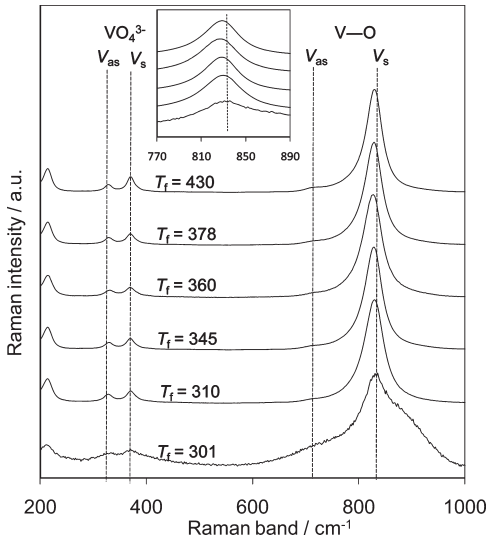

Figure 4. Raman spectra of $BiVO_4$ nanoparticles excited by a green laser (514 nm). Inset shows an enlarged image of the gradual shift in V—O (V_s) band position with increasing T_f (in °C).

Table 3. Raman Peak Position, V—O bond length and optical band gap energy of flame-Synthesized and HNO_3 Solution-Modified $BiVO_4$ Nanoparticles

sample	T_f (°C)	Raman band (cm^{-1})	V—O bond length (Å)[a]	bandgap (eV)
1	301	835	1.689	2.56
2	310	829	1.694	2.64
3	345	829	1.694	2.67
4	360	827	1.695	2.67
5	378	827	1.694	2.67
6	430	827	1.694	2.66
7	$mBiVO_4$-1a	826	1.696	2.60
8	$mBiVO_4$-1b	826	1.696	2.59
9	$mBiVO_4$-2b	826	1.696	2.61

[a] $\nu\ (cm^{-1}) = 21349 \exp[-1.9176\ R(Å)]$.[29,30]

can be estimated from the absorption edges ($\alpha h\nu = A(h\nu - E_g)^n$), where $n = 2$ for direct semiconductors.[31] The estimated bandgap energies for $BiVO_4$ typically increases (blue shift) from 2.56 eV for the predominantly amorphous sample (T_f = 301 °C) to 2.67 eV for fully crystallined samples (Table 3). The bandgap values of these as-prepared $BiVO_4$ nanocrystals are generally larger than the reported values of 2.20—2.36 eV for submicrometer crystals.[6,24,32] Higher bandgap energies for flame-synthesized $BiVO_4$ particles may be ascribed to "quantization-like" effect[9] or absorbed water molecules on the particle surface.[32] In the latter case, adsorbed water molecules (as commonly associated with wet preparation techniques) on Bi sites have been predicted by first principle calculation to decrease the bandgap energy of $BiVO_4$.[33] It is argued here that water adsorption is less significant in flame synthesis. Postannealing of the as-prepared $BiVO_4$ at 300 °C did not result in the reduction of bandgap. As will be shown later (Section 3.3), although modification of the flame-made $BiVO_4$ by aqueous technique did slightly lower the measured bandgap as a result of adsorbed water molecules, the overall bandgap is still significantly larger than that reported for

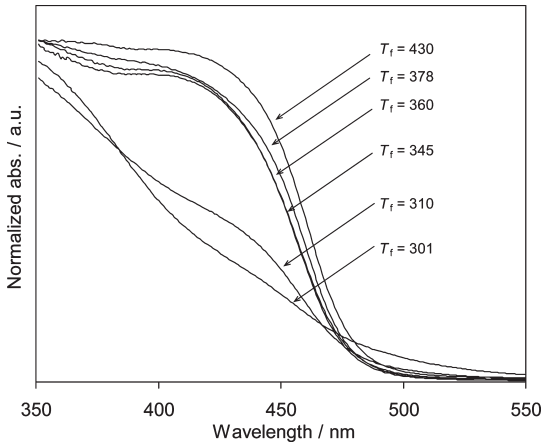

Figure 5. UV—vis diffuse-reflectance spectra of flame-prepared $BiVO_4$ samples of different exposed filter temperatures (T_f in °C).

bulk crystals, corroborating the existence of "quantization-like" effects in these flame-derived $BiVO_4$ nanoparticles.

3.2. Photocatalytic Oxygen Evolution from Flame-Synthesized $BiVO_4$ Photocatalysts. The photocatalytic activity of as-synthesized $BiVO_4$ photocatalysts was assessed for the oxygen evolution reaction from aqueous solution containing $AgNO_3$ as electron acceptor. As shown in Figure 6a, gaseous oxygen is generated from all catalysts except for the predominantly amorphous sample (i.e., T_f = 301 °C). In fact, systematic enhancement in O_2 evolution rates was measured for all samples with increasing T_f, demonstrating unambiguously the importance of $BiVO_4$ crystallinity and scheelite-monoclinic contents. The presence of amorphous content is usually associated with recombination of photoexcited electrons and holes,[34,35] whereas only the scheelite-monoclinic phase was reportedly active for photocatalytic reactions under visible light.[14] That the increase in O_2 evolution activity behaves in opposite trend to the specific surface area infers the more important factor of the quality of the active sites, that is, highly crystallined scheelite-monoclinic sites, as opposed to having more surface areas. Note: Although exposing $BiVO_4$ to higher T_f may give rise to more active photocatalyst samples, higher temperatures than T_f = 430 °C could not be achieved in the current setup because of severe sintering of deposited $BiVO_4$ and the glassfiber filter, which prevented recovery of $BiVO_4$ powders.

As-collected amorphous $BiVO_4$ (T_f = 301 °C) particles were calcined at different temperatures, T_c = 300, 450, and 550 °C, to simulate the effects of different T_f. Full crystallinity was achieved in all cases (see Figure S1 and Table S1 in the Supporting Information) after relatively long calcination time of 6 h (as compared to just 15 min exposure during flame synthesis). Scheelite-monoclinic content of 87, 89 and 100% was attained at T_c = 300, 450, and 550 °C, respectively (see Table S1 in the Supporting Information). Because full crystallinity was attained even at T_c = 300 °C (while T_f = 301 °C was predominantly amorphous), the sample exhibited reasonable activity in photocatalytic O_2 evolution (Figure 6b). The highest activity was measured for sample with T_c = 450 °C. By comparison however, the photocatalytic activity of these calcined catalysts were significantly less than the equivalent fully crystallined, 89% scheelite-monoclinic obtained by as-collected $BiVO_4$ (T_f = 360 °C). This could arise from the decreased SSA and perhaps more significantly due to the formation of oxygen vacancy defects

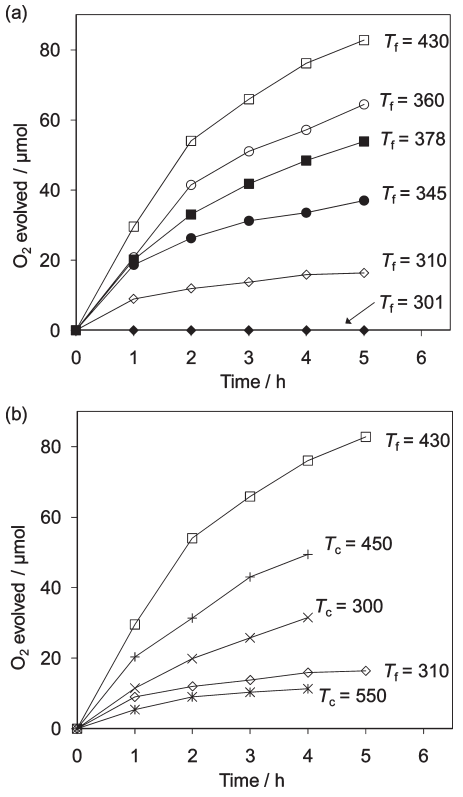

Figure 6. Photocatalytic oxygen evolution from (a) flame-synthesized $BiVO_4$ (T_f, temperature at the filter paper, in °C) and (b) calcined $BiVO_4$ (T_c, furnace temperature during calcination, in °C). Catalysts, 0.3 g $BiVO_4$; solution 0.05 M $AgNO_3$; light source, 300 W Xe lamp with 420 nm cutoff filter; reaction cell, top irradiation cell with a Pyrex window. Note: The decreased rate of O_2 evolution towards the end of experiment is due to exhaustion of Ag^+ electron scavenger.

upon heat treatment,[36] the latter of which is evident from the red shift in absorption threshold and tailing absorption in the visible light range (see Figure S2 in the Supporting Information). These effects were even more pronounced for sample T_c = 550 °C, which further led to significant decrease in O_2 evolution activity.

3.3. Aqueous Modification of Flame-Made $BiVO_4$ Nanoparticles. Given that the source of low photocatalytic activity in flame-derived and heat-treated samples were identified in the above section, here, an aqueous-based acid modification is designed to reconstruct the $BiVO_4$ surface as well as to assist its crystallization aging.[37] To demonstrate this, amorphous $BiVO_4$ particles (T_f = 301 °C) were aged in aqueous nitric acid solution (0.75 M). Acidic solution with pH <2 was necessary to achieve partial Bi solubility and speciation of V as vanadyl ions (VO_2^+) during its crystallization-reconstruction.[37] Extensive particle growth (presumably by coalescence) occurs during such treatment, leading to a significant loss in SSA from 28 to 7 $m^2\ g^{-1}$. Rietveld analysis on the modified $BiVO_4$ (hereby denoted as $mBiVO_4$-1a) reveals only the scheelite-monoclinic phase (Figure 7, Table 1), as coherent with the surface Raman analysis (Figure 8). The average V−O bond length was altered from 1.689 to 1.696 Å, as expected for the transformation from amorphous to scheelite-monoclinic phase. More importantly, this points to the crystallization process of $BiVO_4$ particles in the acidic aqueous solution, further allowing relocation of Bi^{3+} ions along the *c*-axis and resulting in a distorted $BiVO_4$ unit cell, that is, the

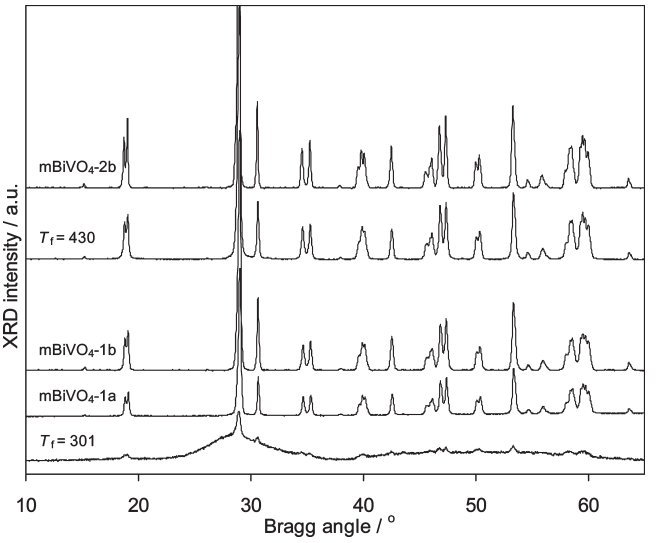

Figure 7. XRD patterns of flame-prepared amorphous $BiVO_4$ (T_f = 301 °C) and that after aqueous treatment without ($mBiVO_4$-1a) and with ($mBiVO_4$-1b) additional of Bi + V precursors. Also shown is the flame-prepared crystalline $BiVO_4$ (T_f = 430 °C) and that after aqueous treatment in the presence of additional Bi + V ($mBiVO_4$-2b).

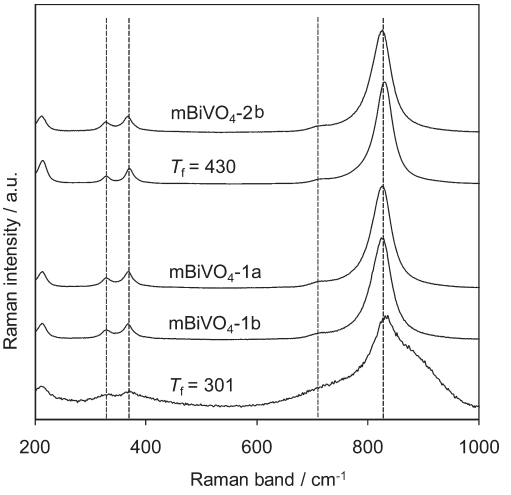

Figure 8. Raman spectra of aqueous treated $BiVO_4$ nanoparticles in comparison to flame-synthesized particle.

monoclinic unit cell structure.[38] The photocatalytic O_2 evolution activity of the most active as-prepared flame $BiVO_4$ sample (T_f = 430 °C) was improved by 20% after the aqueous acid treatment (Figure 9).

To achieve more effective reconstruction of the flame-made $BiVO_4$ surface, we added a small amount of Bi and V precursors (0.01 mM each in metal concentration) during aqueous modification. The treatment was carried out on two different flame-synthesized $BiVO_4$ samples (T_f = 301 and 430 °C; denoted as $mBiVO_4$-1b and $mBiVO_4$-2b, respectively after modification). The additional Bi and V precursors were to eradicate crystal defects originating from the volatility of the metals during exposure to heat (from the spray flame).[39] As shown from the XRD (Figure 7, Table 2) and Raman spectra (Figure 8), a fully crystallined scheelite monoclinic phase, indifferent from $mBiVO_4$-1a was

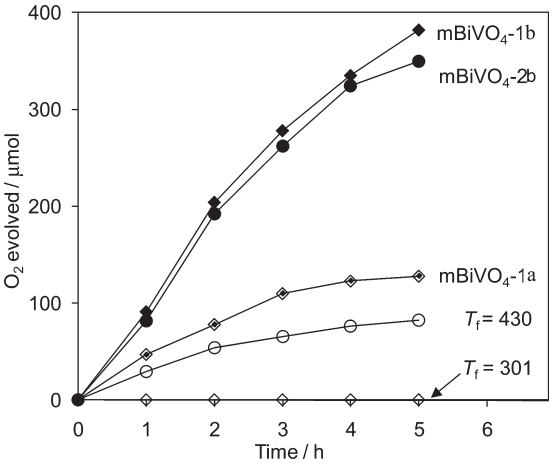

Figure 9. Enhanced photocatalytic oxygen evolution of aqueous modified $BiVO_4$ photocatalysts with additional Bi + V precursors ($mBiVO_4$-1b,2b) under visible light ($\lambda > 420$ nm) radiation, in comparison to aqueous acid treatment without additional precursors ($mBiVO_4$-1a). As-prepared amorphous ($T_f = 301$ °C) and crystallined ($T_f = 430$ °C) $BiVO_4$ are shown as comparisons. Note: The decreased rate of O_2 towards the end of experiment evolution is due to exhaustion of Ag^+ electron scavenger.

obtained. Although it has been reported that plate-shaped $BiVO_4$ can be prepared from aqueous nitric acid containing Bi and V precursors,[14,40] they are not observed in both $mBiVO_4$-1b and $mBiVO_4$-2b (SEM not shown). In other words the added small amount of Bi and V precursors were mainly used for the reconstruction of $BiVO_4$ surface, not for the evolution of new $BiVO_4$ particles. Additionally, the fact that the amorphous $BiVO_4$ ($T_f = 301$ °C) is crystallized in HNO_3 indicates that the aqueous treatment also affects bulk properties of $BiVO_4$. Compared to the as-prepared $BiVO_4$ (2.67 eV), the measured bandgap energy of aqueous-modified $BiVO_4$ was slightly lowered (2.59−2.61 eV). This may be attributed to adsorbed moisture (as a result of aqueous treatment, as discussed earlier), as well as the reduction in crystal and oxygen vacancy defects.

Figure 9 shows the photocatalytic oxygen evolution of $BiVO_4$ after aqueous acid treatment with additional Bi and V precursors. The improvement is almost 5 fold, compared to the most active sample, achievable by flame synthesis alone, i.e., $T_f = 430$ °C. The photocatalytic activity of these two aqueous-treated samples (with additional Bi and V) was comparable regardless of the initial starting $BiVO_4$ material be it amorphous or crystallined samples, suggesting similar extent of crystallization and reconstruction during the treatment.

Figure 10a shows the photocurrent response (J) of crystalline flame-made $BiVO_4$ (T_f = 430 °C) before and after aqueous treatment. It is evident that the photocurrent density in modified $BiVO_4$ photocatalysts ($mBiVO_4$-2b, J_2 = 3.8 μA cm^{-2}) is almost double, relative to the as-prepared flame sample (J_1 = 1.7 μA cm^{-2}), corroborating the higher photocatalytic O_2 evolution activity. More importantly, the former shows negative shifting of the onset potential by 0.05 V. In other words, the charge-trapping defects (sub-bandgap defects, e.g., oxygen vacancies) in the treated sample were reduced after aqueous treatment, hence allowing the quasi-Fermi level to move closer to the conduction band edge of the $BiVO_4$. Figure 10b compares the photoelectrochemical measurement of the two modified $BiVO_4$ samples without ($mBiVO_4$-1a) and with ($mBiVO_4$-1b) the addition of Bi and V salts; the starting

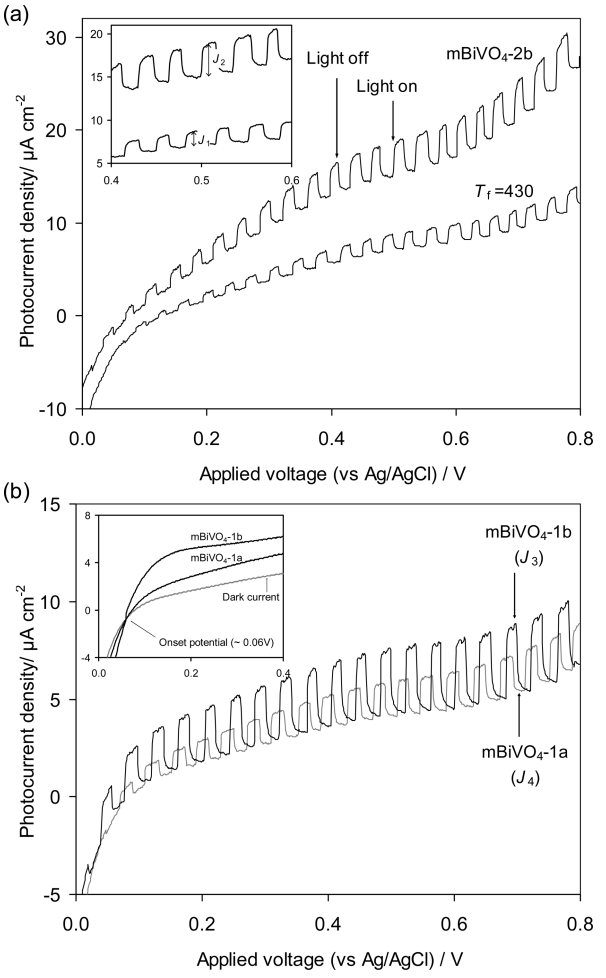

Figure 10. Comparison of photoresponse of (a) as-prepared $BiVO_4$ (T_f = 430) and that after aqueous treatment ($mBiVO_4$-2b); and of (b) aqueous-modified $BiVO_4$ without ($mBiVO_4$-1a) and with ($mBiVO_4$-1b) additional Bi + V precursors.

particles were of amorphous nature initially. Both samples show the same onset potential of 0.06 V (see inset of Figure 10b), inferring similar bulk electronic properties in both cases. However, sample $mBiVO_4$-1b which was treated with additional precursors exhibits higher photocurrent density (J_3 = 3.3 μA cm^{-2}), as compared to sample $mBiVO_4$-1a (J_4 = 1.8 μA cm^{-2}). The higher photocurrent density in the former is in agreement with the enhanced photocatalytic O_2 evolution. The measurements imply that while the aqueous treatment promotes the crystallization of $BiVO_4$, additional Bi and V were important in restoring stoichiometric of $BiVO_4$ without affecting the overall electronic properties.

4. CONCLUSIONS

In this work, we investigated the evolution of crystallization and phase transformation of $BiVO_4$ nanoparticles on the collection filter as a function of exposed temperatures from the aerosol-laden flame itself. Simultaneous crystallization and phase transformation from scheelite-tetragonal to scheelite-monoclinic occurs above 300 °C. Although postcalcination of the flame-made $BiVO_4$ samples could also promote analogous crystallization and phase transformation, the induced defects e.g. oxygen vacancies and stoichiometric defects were highly detrimental to the

photocatalytic activity. The findings imply that the general high temperature synthesis of active $BiVO_4$ photocatalysts, beyond flame synthesis, e.g. chemical vapor deposition, solid-state reaction, spray pyrolysis, etc., requires the balancing of temperature and duration (to achieve high crystallinity and scheelite-monoclinic) with materials stability (induced defects and crystal size).

To circumvent the shortcomings of the flame synthesis, treatment in aqueous nitric acid was applied to the flame-made $BiVO_4$ samples to enhance their crystallinity and phase transformation. However, only marginal improvement in photocatalytic activity relative to the most active as-prepared $BiVO_4$ results, most likely due to the existence of stoichiometric defects. Hence, addition of small amount of Bi and V precursors during the aqueous treatment drastically improved the photocatalytic O_2 evolution rates by 5 folds. The facile post-treatment demonstrates the ability to activate $BiVO_4$ nanoparticles with low crystallinity and high defect content.

■ ASSOCIATED CONTENT

Supporting Information. XRD patterns and Rietveld analysis of flame synthesized $BiVO_4$ powders after calcinations at 300−550 °C. This material is available free of charge via the Internet at http://pubs.acs.org.

■ AUTHOR INFORMATION

Corresponding Author
*E-mail: r.amal@unsw.edu.au. Fax: +61 2 9385 5966.

■ REFERENCES

(1) Bierlein, J. D.; Sleight, A. W. *Solid State Commun.* **1975**, *16*, 69.
(2) Lu, T.; Steele, B. C. H. *Solid State Ionics* **1986**, *21*, 339.
(3) Shanta, K.; Varma, K. B. R. *Mater. Sci. Eng., B* **1999**, *60*, 66.
(4) Smith, H. M. *High Performance Pigments*; Wiley-VCH: Weinheim, Germany, 2002.
(5) Manolikas, C.; Amelincks, S. *Phys. Status Solidi A* **1980**, *60*, 167.
(6) Kudo, A.; Ueda, K.; Kato, H.; Mikami, I. *Catal. Lett.* **1998**, *53*, 229.
(7) Kato, H.; Hori, M.; Konta, R.; Shimodaira, Y.; Kudo, A. *Chem. Lett.* **2004**, *33*, 1348.
(8) Kudo, A.; Miseki, Y. *Chem. Soc. Rev. B* **2009**, *38*, 253.
(9) Iwase, A.; Kudo, A. *J. Mater. Chem.* **2010**, *20*, 7536.
(10) Kohtani, S.; Koshiko, M.; Kudo, A.; Tokumura, K.; Ishigaki, Y. *Appl. Catal., B* **2003**, *46*, 573.
(11) Kohtani, S.; Tomohiro, M.; Tokumura, K.; Nakagaki, R. *Appl. Catal., B* **2005**, *58*, 265.
(12) Long, M.; Cai, W.; Cai, J.; Zhou, B.; Chai, X.; Wu, Y. *J. Phys. Chem. B* **2006**, *110*, 20211.
(13) Kudo, A.; Omori, K.; Kato, H. *J. Am. Chem. Soc.* **1999**, *121*, 11459.
(14) Tokunaga, S.; Kato, H.; Kudo, A. *Chem. Mater.* **2001**, *13*, 4624.
(15) Lim, A. R.; Choh, S. H.; Jang, M. S. *J. Phys.: Conds. Matter* **1995**, *7*, 7309.
(16) Galembeck, A.; Alves, O. L. *Thin Solid Films* **2000**, *265*, 90.
(17) Zhang, L.; Chen, D. R.; Jia, X. L. *J Phys. Chem. B* **2006**, *110*, 2668.
(18) Zhou, L.; Wang, W.; Liu, S.; Zhang, L.; Xu, H.; Zhu, W. *J. Mol. Catal. A* **2006**, *252*, 120.
(19) Yu, J.; Kudo, A. *Adv. Func. Mater.* **2006**, *16*, 2163.
(20) Strobel, R.; Metz, H. J.; Pratsinis, S. E. *Chem. Mater.* **2008**, *20*, 6346.
(21) Castillo, N. C.; Heel, A.; Graule, T.; Pulgrain, C. *Appl. Catal., B* **2010**, *95*, 335.
(22) Teoh, W. Y.; Amal, R.; Mädler, L. *Nanoscale* **2010**, *2*, 1324.
(23) Teoh, W. Y.; Mädler, L.; Beydoun, D.; Pratsinis, S. E.; Amal, R. *Chem. Eng. Sci.* **2005**, *60*, 5852.
(24) Schulz, H.; Mädler, L.; Strobel, R.; Jossen, R.; Pratsinis, S. E.; Johannessen, T. *J. Mater. Res.* **2005**, *20*, 2568.
(25) Zhou, L.; Wang, W.; Zhang, L.; Xu, H.; Zhu, W. *J. Phys. Chem. C* **2007**, *111*, 13659.
(26) Mädler, L.; Pratsinis, S. E. *J. Am. Ceram. Soc.* **2002**, *85*, 1713.
(27) Liu, J. B.; Wang, H.; Wang, S.; Yan, H. *Mater. Sci. Eng., B* **2001**, *104*, 36.
(28) Gotic, M.; Music, S.; Ivanda, M.; Soufek, M.; Popovic, S. *J. Mol. Struct.* **2005**, *744*, 535.
(29) Brown, I. D.; Wu, K. K. *Acta Crystallogr., Sect. B* **1976**, *32*, 1957.
(30) Franklin, D. H.; Wachs, I. E. *J. Phys. Chem.* **1991**, *95*, 5031.
(31) Walsh, A.; Yan, Y.; Huda, M. N.; Al-Jassim, M. M.; Wei, S.-H. *Chem. Mater.* **2009**, *21*, 547.
(32) Li, G.; Zhang, D.; Yu, J. C. *Chem. Mater.* **2008**, *20*, 3983.
(33) Oshikiri, M.; Boero, M. *J. Phys. Chem. B* **2006**, *110*, 9188.
(34) Ohtani, B.; Bowman, R. M.; Colomno, D. P.; Kominami, H.; Noguchi, H.; Uosaki, K. *Chem. Lett.* **1998**, *27*, 579.
(35) Ikeda, S.; Sugiyama, N.; Murakami, S.; Kominami, H.; Kera, Y.; Noguchi, J.; Uosaki, K.; Torimoto, T.; Ohtani, B. *Phys. Chem. Chem. Phys.* **2003**, *5*, 778.
(36) Hirota, K.; Komatsu, G.; Yamashita, M.; Takemura, H.; Yamaguchi, O. *Mater. Res. Bull.* **1992**, *27*, 823.
(37) Wood, P.; Glasser, F. P. *Ceram. Int.* **2004**, *30*, 875.
(38) Sleight, A. W.; Chen, H.-Y.; Ferretti, A.; Cox, D. E. *Mater. Res. Bull.* **1979**, *14*, 1571.
(39) Sun, Y.; Xie, Y.; Wu, C.; Long, R. *Cryst. Growth Des.* **2010**, *1*, 602.
(40) Iwase, A.; Kato, H.; Kudo, A. *J. Sol. Energy Eng.* **2010**, *132*, 021106.